Cyclic CO_2 – H_2O injection and residual trapping: implications for CO_2 injection efficiency and storage security

Edlmann K.[1], Hinchliffe S.[1], Heinemann N.[1], Johnson G.[1], Ennis-King J.[2] and McDermott C.I.[1]

[1]*School of GeoSciences, University of Edinburgh, Grant Institute, The King's Buildings, University of Edinburgh, James Hutton Road, Edinburgh, EH9 3FE. United Kingdom.*

[2]*CSIRO Energy, Private bag 10, Clayton South VIC 3169, Australia.*

Corresponding Author

Katriona Edlmann: School of Geoscience, Grant Institute, The King's Buildings, University of Edinburgh, James Hutton Road, Edinburgh, EH9 3FE, United Kingdom.

kedlmann@staffmail.ed.ac.uk

Telephone: +44 (0) 131-650-7339

Fax: +44 (0) 131-668-3184

Graphical abstract

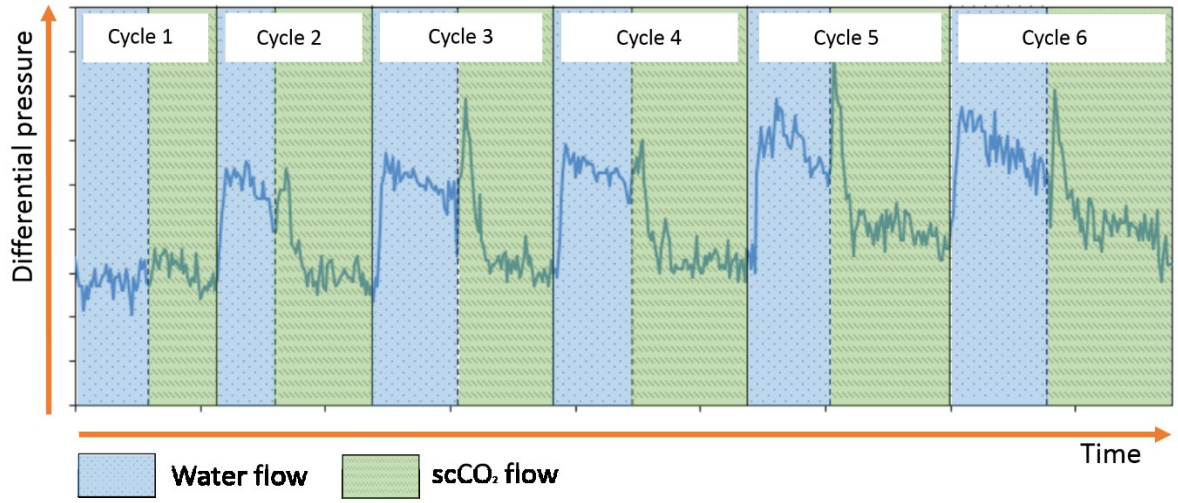

Abstract

To meet the Paris Agreement target of limiting global warming to 2ºC or below it is widely accepted that Carbon Capture and Storage (CCS) will have to be deployed at scale. The influence of residual trapping on CO_2 well injectivity and its response over time has a major impact on the injection efficiency and storage capacity of CO_2 storage sites. For the first time, experiments have been undertaken over six cycles of water and supercritical CO_2 injection using a state of the art high flow rig recreating in-situ conditions of near wellbore injection into analogue storage reservoir rocks. The results show that differential pressure continuously increases over multiple injection cycles. Our interpretation is that multiple cycles of injection results in a reduced effective permeability due to increased residual trapping acting as a barrier to flow resulting in reduced injectivity rates. This is supported by numerical modelling and field observations that show CO_2 injectivity and its response over time will be affected by multiple cycles of injection. These results suggest that loss of injectivity must be incorporated into the injection strategy and that careful management of cyclic injection will create the opportunity to increase residual trapping.

1. Introduction

The injection and storage of CO_2 into deep saline aquifers could make a significant contribution to reducing global greenhouse emissions (Bachu and Adams, 2003; Benson and Cole, 2008; Edlmann et al., 2015; IEA, 2004; Koide et al., 1992; Metz, Davidson, de Coninck, 2005). Current field experience (Alcalde et al., 2017; Hosa et al., 2010) suggests that a single well can inject in excess of 1MT of CO_2 per year with numerical simulations indicating that during constant CO_2 injection, these injectivity rates can be maintained (Heath et al., 2014; Jikich et al., 2003; Rutqvist et al., 2008; Zoback and Gorelick, 2012). However, due to multiple input sources of CO_2, alternating CO_2 / brine injection strategies, periodic injection and varying injection rates along with well maintenance and workovers, a constant maintained injection strategy over a ~30 year project lifetime is unlikely. Field experience from CO_2-EOR projects using water alternating gas injection (WAG) have shown that a 20% loss of injectivity over the well life can be expected (Potter et al., 1992; Schneider and Owens, 1976; Sohrabi et al., 2005). This suggests that ensuring CO_2 injectivity can be maintained will require careful understanding of the fluid pressure response to cyclic injection over time (Burton et al., 2008). Fluid mobility has a direct impact on the injectivity of a well, because fluid mobility is reduced in a multiphase system leading to higher fluid pressures (Bachu, 2008; Dullien, 1992; Edlmann et al., 2013; Heinemann et al., 2012; Morris et al., 2011). This means that to maintain infection rates higher pressures will be experienced, limited by fracture pressure, which if exceeded has the potential to open flow paths through which the CO_2 could escape (Edlmann et al., 2016; McDermott et al., 2013; Smart et al., 2001).

The limited cyclic CO_2 / water (or brine) injection experiments on the multiphase flow characteristics of CO_2 injection in the literature generally do not extend beyond two cycles (Edlmann et al., 2013; Gamadi et al., 2014; Grigg and Svec, 2006, 2007; Larsen A., 1995; Ma et al., 2016). Saeedi et al. undertook four cycles of injection and found that there were notable hysteresis effects on injectivity during cyclic CO_2 - brine injection (Saeedi et al.,

2011). They suggested that this hysteresis effect may be limited to the first and second flooding cycles.

In this paper, we present the results of six cycles of CO_2 - brine injection. Our experiments have been designed using water unsaturated with respect to CO_2 to concentrate our focus on the near well bore injection area and in particular the response of the bottom hole / injection pressure. We find that for both the CO_2 and water injection cycles, the differential pressure increases with each injection cycle and that the hysteresis effect is progressive. Fluid mobility, which controls the differential pressure in the experiments, is influenced by (1) pore space geometry, (2) wettability characteristics, and (3) the residual saturation of each fluid phase. We investigate all three aspects to determine which is responsible for the increase in differential pressure and confirm our interpretation by numerically simulating the experiments and by reviewing real world CO_2 injection operations.

2. Materials and methods

The experimental rig was designed to recreate subsurface near wellbore CO_2 injection conditions. The equipment consists of a Hassler-type pressure vessel which holds cylindrical rock samples of 38mm diameter within a pressurised rubber sleeve that applies the confining pressure. A pair of Teledyne ISCO syringe pumps at the upstream end of the fluid system control the flow rate of CO_2 and a HPLC water pump controls the flow rate of water. A second pair of syringe pumps on the downstream end of the fluid system work in constant pressure mode to control the fluid pressure. The core holder is contained within an oven, allowing the temperature of the sample to be controlled and maintained. Full details of the experimental equipment and considerations are given in the Supporting Information (SI). Saturation tracking and fluid collection was not possible within the experimental setup. To recreate subsurface injection conditions as closely as possible, the experiment was run with supercritical phase CO_2. To achieve this, the rock and fluid temperature was set to 40^{o}C, the pore / fluid pressure at 10MPa, the confining pressure at 20MPa and the flow rate for both the water and CO_2 pumps set to 1ml/min.

2.1. Experimental methodology

After injecting water though the sample to steady state flow for at least 15 minutes (primary imbibition phase), the water injection is stopped and CO_2 injection initiated (primary drainage phase), maintaining steady state CO_2 injection for at least 15 minutes. The second cycle then begins by stopping the CO_2 injection and re-initiating the water injection (secondary imbibition phase), maintaining steady state water injection for at least 15 minutes followed by CO_2 injection (secondary drainage phase), again maintaining steady state CO_2 injection for at least 15 minutes. This sequence was repeated for six cycles of alternating CO_2 and water injection. The detailed experimental process cycle for the flow experiments and the exact timings of the flow cycles are provided in the SI.

2.2. Fluid properties

The two fluids used during the cyclic experimental work were de-ionised water (unsaturated with respect to CO_2) as a proxy for brine and supercritical CO_2. The mass flow rate of water is in parity with the volumetric flow rate, assuming at 40^{o}C and 10MPa the water density is 992.2kg/m^3 and dynamic viscosity is 6.53 x10^{-4}Pa.s (Suekane, 2008). The ISCO CO_2 syringe pump pressure was maintained at 10MPa and at a temperature of 5^{o}C to ensure pump efficiency (CO_2 density of 947.3kg/m^3 at 10MPa and 5^{o}C) therefore the mass flow rate leaving the pump is close to 1ml/min. However the temperature of the CO_2 fluid entering the core sample passes through a heat exchanger at oven at 40^{o}C where the CO_2 density is 628.7kg/m^3 at 10MPa with a dynamic viscosity of 4.82 x10^{-5}Pa.s. This results in a change in the volumetric flow rate through the sample. The flow rate of CO_2 through the sample was estimated using mass conservation from the pump mass flow rate (1ml/min) multiplied by the density ratio of the syringe pump CO_2 over the sample inlet CO_2 (947.3 / 628.7 = 1.5), resulting in a volumetric flow rate for CO_2 into the sample of 1.5ml/min.

The solubility of CO_2 is controlled by temperature, pressure and concentration of dissolved matter. Under the experimental conditions the CO_2 solubility is approximately 54.9kg per

1000kg of unsaturated water, so 1 pore volume of water can dissolve 0.087 pore volumes of CO_2.

2.3. Sample Characterisation

The experiment was conducted on Fell sandstone, a homogeneous quartz rich sandstone and suitable UK North Sea aquifer storage analogue (Heinemann et al., 2013; Lewicki et al., 2007; McDermott et al., 2017). It was chosen as it has an open pore network and is primarily composed of quartz, minimising potential for significant capillary pressure or mineral reactivity influences, thereby enabling us to concentrate on the multiphase fluid response.

The experiment was conducted on a 38mm diameter and 80mm long cylindrical sample of Fell sandstone, with a helium porosity of 20.3%, implying a pore volume of 18.4ml. The sample intrinsic permeability to water of 26.24mD was measured at the beginning of the experiment.

2.4. Sample mineralogy

The mineralogical composition of the sandstone was determined using X-Ray Diffraction (XRD) before and after the experiment, supplemented by optical microscopy and Scanning Electron Microscope (SEM) investigations to assess whether there was chemical reactivity that could impact on the pore space geometry. The Fell sandstone is primarily quartz (93%) with microcline (2%), illite (1.2%), kaolinite (1%) and calcite (0.1%). Detailed SEM images and the XRD mineral abundances before and after the experiment are given in the SI.

2.5. Pore space geometry analysis

There is a large body of work that relates pore size and shape to capillary pressure, relative permeability and hysteresis, where capillary pressure decreases as pore throat radius increases (Doyen, 1988; DULLIEN, 1992; Garcia et al., 2009; Jerauld and Salter, 1990; Pittman, 1992). Pore shape analysis of the Fell sandstone was calculated on four images over three magnifications obtained from the optical microscope (OM) and backscattered (BS) SEM images. The results show that the Fell sandstone has interconnected relatively

wide pore throats and moderately well rounded macro pores, within the 100μm to 400μm size range. The smaller pores are simple and well-rounded becoming more complex with increasing size. This implies that the influence of pore geometry does not inhibit fluid mobility, hence its influence on fluid flow characteristics will be minimal and will not significantly influence the effective permeability results. Full details of the pore space geometry analysis are presented in the SI.

2.6. Numerical simulation

Cyclic injection of different fluid phases will cause a hysteresis effect. Capillary forces within each of the drainage and imbibition cycles cause some of the non-wetting CO_2 to become disconnected, through snap-off, immobilised and residually trapped.

The first part of the numerical modelling fits a hysteretic model directly to the experimental data, in order to judge whether the observed behaviour fits within a standard paradigm. The hysteretic model for relative permeability and capillary pressure is outlined by Doughty (Doughty, 2007) and implemented in the inverse modelling code iTOUGH2 (Finsterle, 2004). The core is modelled as homogeneous cylinder of rock, and it is assumed that variations in saturation only occur along the axial direction i.e. the problem is one dimensional. The rates and timing of injection of water and CO_2 are taken directly from the experiment, and the experimental pressures are fitted to the model at chosen calibration points (six per cycle) by adjusting the parameters of the hysteresis model through inversion algorithms.

It has been observed in core floods that due to the time scales of CO_2/water equilibration within the pore space relative to the flow velocity, the water that flows out of the core may be less than fully saturated with CO_2. Thus the standard assumption in the simulator of local equilibrium between phases may not reflect the experimental situation, and reduced dissolution could potentially lead to increasing CO_2 saturation across cycles. In these experiments there is no direct measurement of the concentration of CO_2 in the outflow, but the effect of this non-equilibrium can be mimicked in a simple way by reducing the effective

solubility of CO_2 in water. A case is fitted with solubility set to 50% of the bulk value at the experimental P, T conditions.

The second part of the numerical modelling examines whether the observed increase in differential pressure could be due to an enhancement of the hysteresis beyond the model just discussed. An alternative model for CO_2 saturation has been devised in which the residual gas saturation for imbibition is increased for each cycle. The reservoir engineering software Eclipse 300 (Schlumberger) (Heinemann et al., 2016; Pickup et al., 2012), was used in this study with the CO_2STORE option based on a modified Peng-Robinson equation of state (Peng and Robinson, 1976) that allows for the mutual solubility of CO_2 and water.

Because it is the purpose of the simulations to show that the differential pressure increase during cyclic CO_2 and water injection can be due to an increase in residual gas saturation, mathematical relative permeability curves adopted from (van Genuchten, 1980) and (Corey, 1954) were used:

$$k_{rl} = \sqrt{S^*}\{1 - (1 - [S^*]^{1/m})^m\}^2 \quad [1]$$

$$k_{rg} = (1 - S')^2(1 - S'^2) \quad [2]$$

Where

$$S^* = (S_1 - S_{lr})/(1 - S_{lr}) \quad [3]$$

$$S' = (S_1 - S_{lr})/(1 - S_{lr} - S_{gr}) \quad [4]$$

The irreducible water saturation (S_{lr}) is initially set to 0.1, the residual gas saturation (S_{gr}) set to 0.05 and the parameter *m* set to 0.6269 according to (Xu et al., 2003) for sand. To model the hysteresis effect during the first injection cycle, the residual gas saturation for imbibition (S_{gri}) was set to 0.2 and is then increased by 0.1 for each cycle (Figure 1). Hence, with increasing model run time the amount of residually trapped CO_2 increases. Capillary pressure has been neglected.

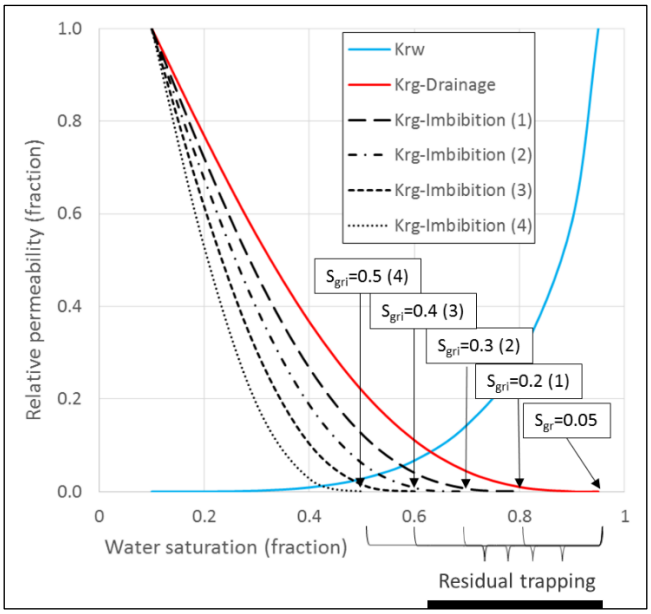

Figure 1 The relative permeability curves for water (krw – blue) and CO_2 (krg – red). The residual saturation for the imbibition process (Sgri) for the four modelled injection cycles increases with every cycle (the cycle number in brackets).

3. Results

3.1. Differential pressure evolution during cyclic CO_2 and water injection

Figure 2 presents the differential pressure response over all six $scCO_2$ / water flow cycle experiments. There is a progressive increase in differential pressure (reduction in fluid mobility) over the six cycles for both fluid phases. For the water phase the average differential pressure nearly doubled from 5.6psi in cycle 1 to 11.3psi in cycle 6. For the $scCO_2$ phase the average differential pressure increased from 6.3psi in cycle 1 to 8.1psi in cycle 6. Interestingly the water, which is considered to be the wetting phase, has a higher differential pressure than the $scCO_2$ and this is explored in more detail in Section 4.

Looking at the results of the water injection cycles (imbibition) in Figure 2 we see that after a $scCO_2$ injection cycle as water is injected there is a sharp increase in differential pressure (decrease in fluid mobility), followed by a slow reduction in differential pressure until the next cycle. For the $scCO_2$ injection cycles (drainage) we see that after a water injection cycle, as $scCO_2$ is injected, there is a significant increase in differential pressure followed immediately

by a sharp fall in differential pressure (an increase in fluid mobility) to a differential pressure below that of the previous water cycle. There is then no significant change in differential pressure over each $scCO_2$ injection period, suggesting that once the $scCO_2$ is connected it maintains a stable flow path.

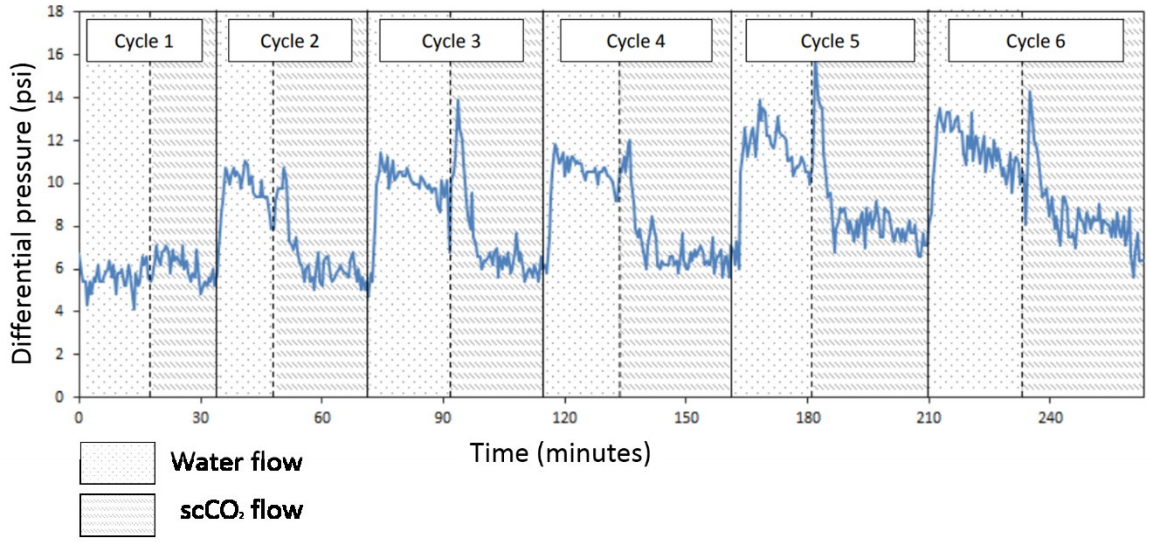

Figure 2 Flow experiment graph of the differential pressure for the Fell Sandstone sample. The cycle number is indicated at the top of the graph. The relevant fluid flow within each cycle is indicated in the key.

3.2. Mineralogy and pore geometry analysis

Full XRD and optical microscopy results for the Fell sandstone for both the pre and post brine - CO_2 flooding experiments are presented in the SI. There is only a small amount of reactive carbonates such as calcite (0.1%) which limits the potential for carbonate dissolution processes within the rock and there are no swelling or reactive clays present (such as montmorillonite) which could have an impact on the flow path of CO_2 by obstructing pore throats through the remobilisation of fine clay particles within the limited timeframe of the experiments (Dávila et al., 2017; Kampman et al., 2014). The post experiment results show minor changes to some minerals after the flow experiments, but in all cases, the percentage mineral change is smaller than the presented standard deviation of the samples. Pre and post experiment optical microscope photographs of the injection surface of the rock

sample also show no mineralogical or thermal alteration within the samples. We conclude that there is minimal mineral reactivity or thermal alteration during the experiment that could alter the pore space, pore throat geometry and as such fluid response. This reinforces our interpretation that the pore geometry does not inhibit or restrict the fluid mobility, and as such, the differential pressure during cyclic CO_2 and water injection.

4. Discussion of results

Wettability is the tendency of one fluid to "wet" or adhere to the surface of a solid in the presence of another immiscible fluid, termed the wetting and non-wetting fluid phase respectively. Wettability can be quantified by determining the contact angle between the wetting fluid and the solid surface involved (Aarnes et al., 2009; DULLIEN, 1992) and therefore is a function of the rock mineralogy as well as the fluid. Wettability of a system may also change with time. The capillary threshold pressure is the pressure that must be overcome before a non-wetting phase will penetrate and flow within the connected pore network and is dependent on the interfacial tension between the wetting and non-wetting fluids, the contact angle between the mineral and fluid phase and the pore throat radius. When a non-wetting phase is injected into a system the differential pressure will increase until the capillary threshold pressure is exceeded. Once the capillary threshold pressure has been exceeded, a continuous migration pathway can be created through which the non-wetting phase can flow and the pressure will drop to an almost constant value. Therefore, the pressure response in the experiments presented here can be used to infer the wettability of the system and whether a change in wettability may be the cause of the increasing pressure observed over the 6 cycles.

Firstly, the magnitude of the differential pressure measured when injecting the two phases (CO_2 and water) could be used to infer the wettability with the lower differential pressure corresponding with the wetting phase. However, this may not be conclusively diagnostic due to other effects discussed below. Secondly, the rate of change of the differential pressure

during the cycle can be used to determine the wetting phase of the experiment. Here, the rate of change of the differential pressure within each cycle can provide an indication of the multiphase flow properties of both the water and $scCO_2$ during each cycle. If the rock and fluid properties are constant, the changes in differential pressures during injection is controlled by capillary pressure and relative permeability. The permeability of one phase at any given location will depend on the saturation of the other phase present along with interactions with the pore network (Aarnes et al., 2009). If water is the wetting phase then in each water flow section, the rate of change of the differential pressure over that period should be faster than for the non-wetting fluid, e.g. CO_2. Lastly, if the wettability changes over time the rate of change in the pressure response in each individual cycle would also change. It has been shown in recent studies that the wettability of quartz surfaces can alter from a strongly water-wet system towards a less water-wet system in the presence of $scCO_2$ (Chiquet et al., 2007; Saraji et al., 2013). As the Fell sandstone is 93% quartz, the possibility of a change in wettability as cause of the change in differential pressure during cyclic injection must thus be taken into account.

In these experiments we predict the water to be the wetting phase. A possible explanation for why the wetting fluid (water) has a higher differential pressure than the non-wetting $scCO_2$ within each cycle could be related to the viscosity difference between the two fluids. The $scCO_2$ is the more mobile phase as it has a lower viscosity (Bachu and Bennion, 2008). This could lead to highly non-uniform displacement of the water leading to channelling of $scCO_2$ through a few preferential flow paths (Saeedi et al., 2011) which could reduce the differential pressure of the $scCO_2$ flow through the samples.

Figure 3 shows the rate of change in pressure in each phase for each cycle. To minimise the effect of any experimental errors during the pump changeovers, the first and last minutes of each cycle were discounted from the rate of change calculations. The median time for each section was found and the ΔP was calculated for the selected time period either side of the

median time and a trendline added with its gradient used to observe changes to the ΔP over time.

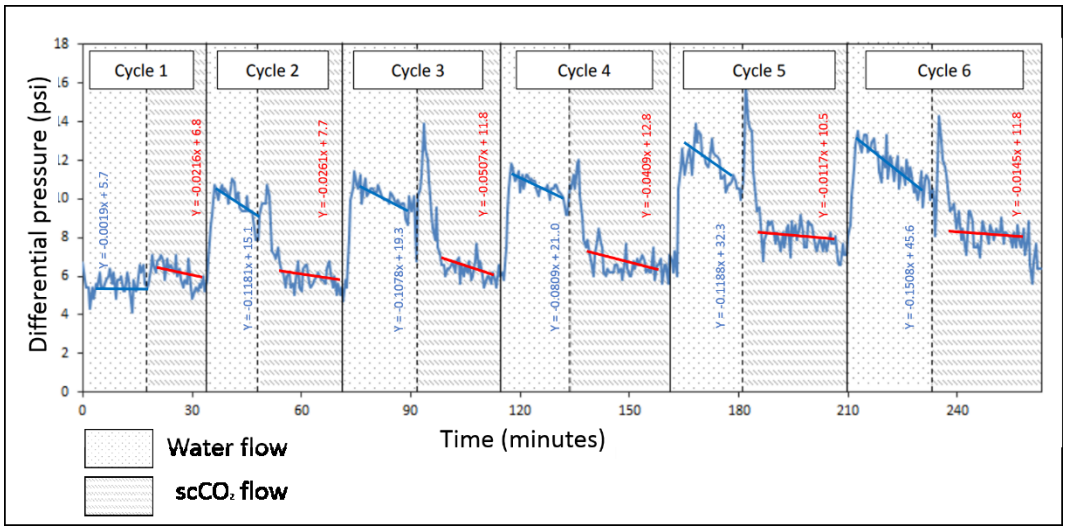

Figure 3 The rate of change in the differential pressure for each fluid flow over all six cycles. The equations for each trendline are shown next to the relevant data.

Figure 2 shows that the reduction of the differential pressure during water injection is relatively steep whereas the pressure during CO_2 injection increases dramatically and then falls to a lower, barely changing level. This indicates that water is the wetting phase and CO_2 is the non-wetting phase throughout the experiments. It is therefore concluded from the rate of change in pressure that the system is indeed water wet and that a wettability change from water-wet to CO_2-wet is not responsible for the continuous increase in differential pressure during cyclic water and CO_2 injection.

4.1. Residual trapping

Within a two phase system the fraction of the pore space occupied by the wetting and non-wetting phase is called the saturation, denoted S_w and S_{CO2} respectively:

$$S_w + S_{CO2} = 1 \qquad [5]$$

Where the non-wetting CO_2 phase can never reach either 0 or 1, due to the wetting water phase adhering to the mineral surfaces. Hence, the two phase system will actually range from the critical water saturation S_{wc} to the maximum water saturation S_w^{max}.

If we consider the typical relative permeability function of water with respect to CO_2 saturation shown in Figure 1, it shows that the less CO_2 present, the higher the wetting phase brine relative permeability, and vice versa. The curve shape is also dependant on flow direction, whether it is undergoing drainage or imbibition. The curves are different as the wetting and non-wetting phase take different flow paths through the network of pores. During drainage the wetting fluid will preferentially fill the smaller pores and pore throats and as the non-wetting fluid begins to flow as a continuous phase through the bigger pores, occupying smaller pores as the non-wetting phase saturation increases. During this drainage cycle, the wetting fluid (water) becomes increasingly reduced and eventually will be present only as a thin film of residual water surrounding the edge of pores, termed irreducible water saturation (S_{ir}). During the imbibition cycle when the wetting phase re-enters the pore network, some of the non-wetting phase becomes gradually disconnected by the wetting phase through capillary snap off and leads to residual trapping as the disconnected non-wetting CO_2 become effectively immobile (Hesse et al., 2009). Each cycle imparts its own change in the fluid saturation profile termed hysteresis (Juanes et al., 2006) which refers to the dependence on the relative permeability to the previous saturation of the sample (Spiteri and Juanes, 2006). Intuitively, as more and more non-wetting CO_2 phase enters through the pore volume, the harder it will be for the wetting water phase to push it all out, as more and more non-wetting CO_2 volume becomes trapped in the smaller pores.

If the injection cycle number is used as a proxy for decreasing water saturation in the core as a result of an increasing amount of residually trapped CO_2 within the pore network, we can create a proxy water relative permeability curve, full details are presented in the SI. The water relative permeability curve shows a gradual decrease in effective permeability with decreasing water saturation (increasing cycle number) which is consistent with the flow

experiment results that indicate that with multiple water / CO_2 injection cycles, increased residual trapping acts as a barrier to flow and plays an important part in controlling multiphase fluid dynamics during cyclic water / CO_2 injection.

This is important as it indicates that over the lifetime of a storage site, experiencing natural cycles of fluid imbibition and drainage, the injectivity of the CO_2 may reduce over time, leading to lower injection rates and/ or increased reservoir pressures.

4.2. Residual saturation simulation analysis

For the first stage of simulation, Figure 4 shows the fitting of a hysteresis model with iTOUGH, where selected pressure points (shown as open circles) are used for the fit. The details of the fitting parameters and the hysteresis model are discussed in the SI. If the data from just the first 4 cycles is used for the inverse model (solid green curve), then the fit is good for those cycles, but doesn't capture the pressures increases especially in the 5th and 6th cycles, particularly during the CO_2 injection stages. Fitting to all 6 cycles doesn't markedly improve the overall quality of fit, and the model is again unable to reproduce the increase in differential pressure over cycles – in each new cycle after the second one, the model gives a very similar result to the previous cycle. This indicates that the hysteresis model is unable to capture some features of the behaviour for multiple injection cycles.

As discussed earlier, the effect of reduced effective solubility is also investigated, since during water imbibition there is dissolution of CO_2 as well as displacement. Injection of water for 30 minutes corresponds to 1.63 pore volumes, which could dissolve 0.14 pore volumes of CO_2 assuming full saturation. The fitted results with the effective solubility at 50% of the bulk value is shown as the dashed black curve. The pressure falloff during the water imbibition stages is flatter in this model (since less CO_2 is dissolved over the injection cycle), but this fails to improve the agreement with the experimental data, and indeed the fitted behaviour of the 3rd-6th cycles closely follows the 2nd cycle. Thus reduced effective solubility is unable to account for the observations.

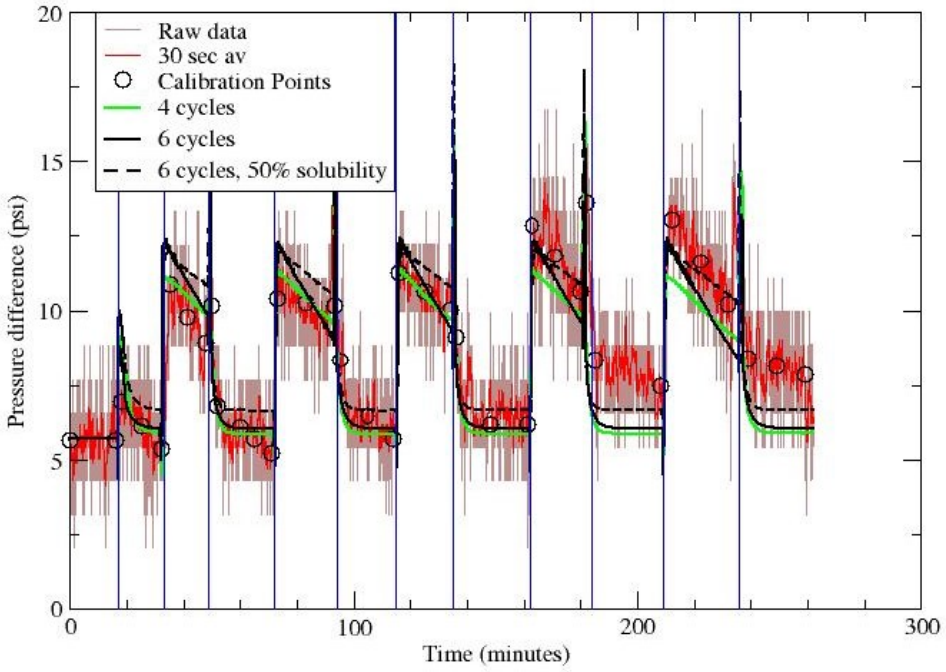

Figure 4 Fitting of the experimental results to a hysteresis model with iTOUGH2. Brown curve: The raw experimental data. Red curves: 30 second average of experimental data. Open circles: calibration points for fit. Solid green curve: hysteresis model fitted to just the first four cycles of water/CO_2 injection. Solid black curve: hysteresis model fitted to all six cycles of water/CO_2 injection. Dashed black curve: hysteresis model fitted to all six cycles of water/CO_2 injection, but with reduced effective solubility 50% of bulk value.

The result of the second stage of modelling, in which the residual trapping in the model is deliberately increased between cycles (Figure 1), is shown in Figure 5. The comparison here is qualitative, in that the simulation model parameters have not been fitted to the data. Two similarities can be observed between the experimental results (Figure 2) and in the modelling results (Figure 5). Firstly, the absolute increase in differential pressure during the water injection period of cycles two, three and four, due to the increasing pore space occupied by residually trapped CO_2 which then has to be pushed out by the invading water. Secondly, the increasing rate of pressure decrease during the water injection period observed in the simulation results can also be seen in the experimental results.

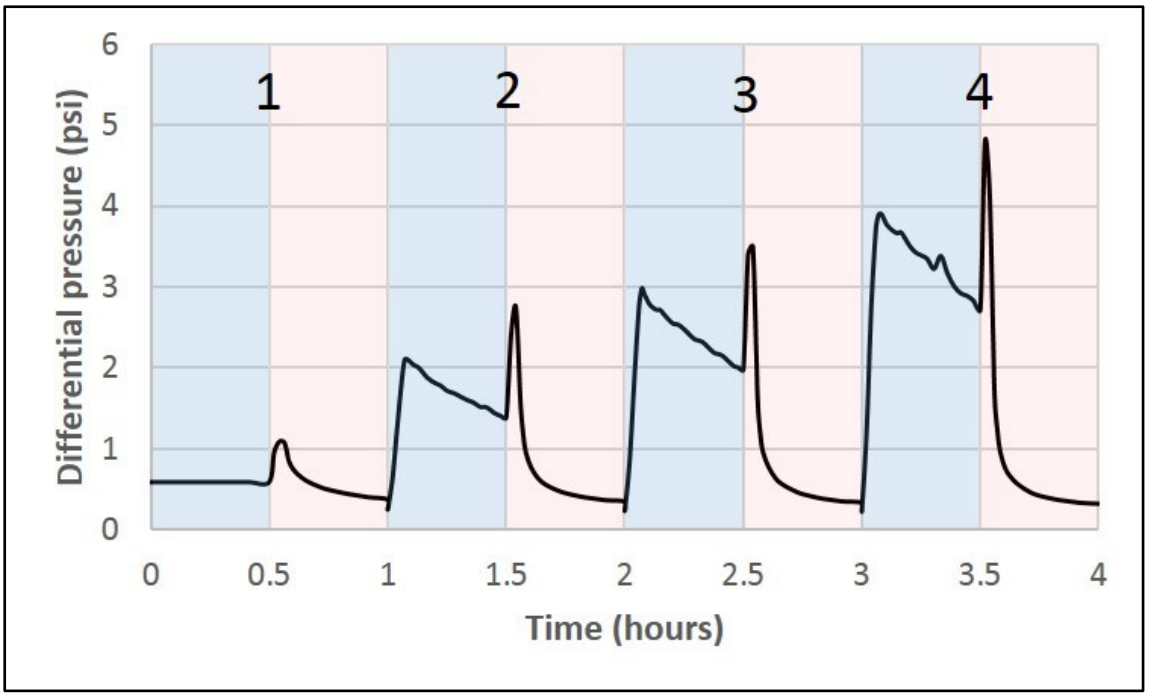

Figure 5 The differential pressure throughout the injection cycles. Periods of water injection are shaded in blue; periods of CO_2 injection are shaded in red. The cycle numbers are highlighted in black, the imbibition residual gas saturation increases with every cycle (see text for more information). Note the increase in differential pressure with increasing cycles.

The simulation results show that an increase in residual CO_2 trapping could lead to an increase in differential pressure during the water injection period. Hence the simulation results are evidence for the hypothesis that a continuous increase of residually trapped CO_2 is responsible for the increase in differential pressure, and indicate that alternative hysteresis models may be needed to incorporate this behaviour in numerical simulations.

4.3. Field observations

Field observations of cyclic water and CO_2 injection are primarily in enhanced oil recovery (EOR) projects where the third fluid phase (hydrocarbon) and production of fluids complicates the interpretation of the pressure profiles as pertaining to residual CO_2 (Eshiet and Sheng, 2014; Gamadi et al., 2014; Hovorka, 2013; Kampman et al., 2014; Meyer, 2005; Müller, 2011). However, a number of field experiments have been performed in CO_2 – brine only systems that allow comparison with the experimental and modelling data presented

here. One of these is the CO2CRC Otway experiment in Victoria, Australia. Here, an engineered residual trapping experiment was conducted twice, once in 2011 and once in 2014 (Ennis-king et al., 2017). The field experiment design is discussed in detail by Zhang et al. (Zhang et al., 2011) but in summary consists of creating a residually trapped CO_2 zone within the formation by following CO_2 injection with CO_2 saturated water injection. Here pressure response was monitored throughout all stages of injection including during baseline characterisation tests (pre CO_2 injection) (Ennis-king et al., 2017). Hence the comparison of pressure profiles during water injection into a water saturated only and residually trapped CO_2 formation is possible. Figure 6 compares the pressure response to water injection before residual CO_2 is present (1^{st} injection) and after it is present (2^{nd} injection) for both the 2011 and 2014 tests. Note that the since the injection rates were not the same each time, the pressures have been scaled to allow a proper comparison. The presence of the residual CO_2 phase significantly increases the pressure build-up which is attributed to the lower relative permeability to water at residual CO_2 saturation. This observation concurs with the results from the modelling and experimental work presented above. The difference between the reservoir response in the 2011 and 2014 tests may be due to alteration of the near-well permeability, possible from sand production (Ennis-King et al., 2017).

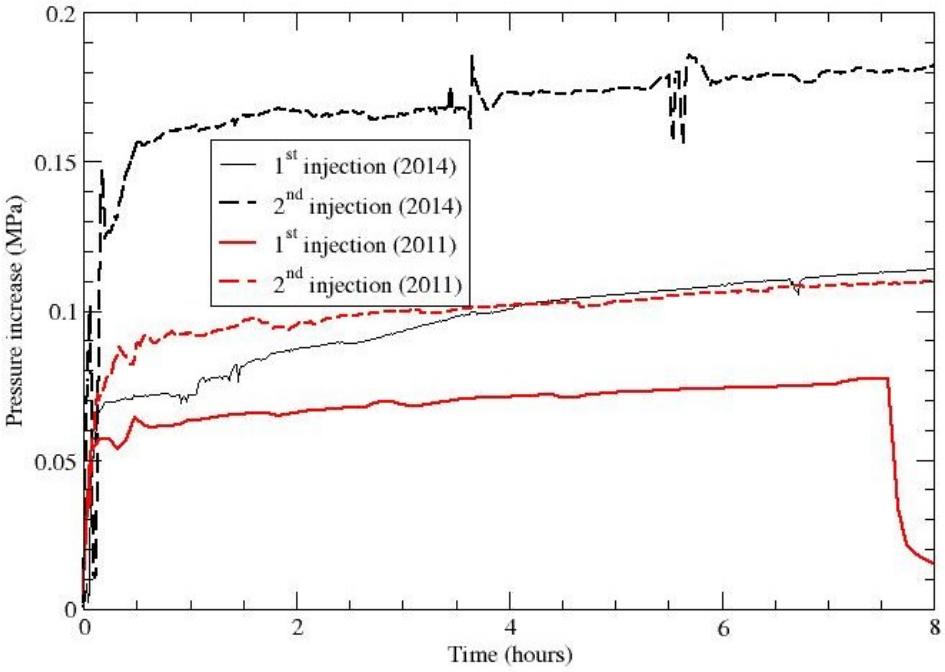

Figure 6 Field data for pressure build-up during water injection before and after CO_2 injection. The single well test was carried out in 2011, and repeated in 2014. Since the injection rates differ for each injection, the pressures have been scaled accordingly. Solid black line: 1st injection (2014), 199 t/day (unscaled). Dashed black line: 2nd injection (2014), rate 155 t/day, pressure scaled by 199/155. Solid red line: 1st injection (2011), 150 t/day, pressure scaled by 199/150. Dashed red line: 2nd injection (2011), 191 t/day, pressure scaled by 199/191.

Modelling of enhanced trapping injection strategies including cyclic CO_2-water at the CO_2 field experiment in Israel (Heletz) (Rasmusson et al., 2016) is presented and discussed in the SI, however field results are not yet published so cannot be further compared here.

5. Conclusions

Our results clearly show, for the first time that the periodic injection of CO_2 over time, be it due to deliberate operational changes or responding to interruptions to CO_2 injection may result in an increase in residually trapped CO_2. This has implications that may benefit or hinder long-term CO_2 storage. On the one hand, increased residual trapping within the same pore space shows increased efficiency of storage operations and hence cost reductions (for

example in monitoring a smaller areal footprint of CO_2 as compared to a plume of the same volume of CO_2 with lower saturations). Increased residual trapping also increases the storage security of an operation due to the reduced buoyant free phase CO_2 that will be present. On the other hand, more residually trapped CO_2 in the vicinity of the well leads to more tortuous flow pathways for the injected CO_2 and hence to a pressure increase that may limit injectivity to within safe bounds. Hence a trade-off occurs between increased pore space utility and security of storage with injectivity and pressure increase. Our results thus will be of import to those deploying large scale and long-term storage and to those who regulate such operations.

6. Acknowledgements

The research leading to these results has received funding from the European Community's FP7 under grant agreement No. 227286, from the European Union's H2020 under Grant Agreement No. 636811, from the European Union's H2020 Accelerating CCS technologies, EPSRC Grant EP/P026214/1 and Data from Stage 2B of the Otway Pilot project has been provided by CO2CRC Ltd, and the field project had support from the Australian National Low Emissions Coal Research and Development (ANLEC R&D).

7. Supporting information

The supporting information contains further detailed information on the experimental equipment, considerations and processes. The sample mineralogy and pore space geometry analysis. The experimental relative permeability, residual saturation hysteresis model and fitting parameters and details of other field examples with CO_2 cyclic flow.

8. References

Aarnes, J.E., Lie, K.-A., Kippe, V., Krogstad, S., 2009. Multiscale methods for subsurface flow. Multiscale Model. ….

Alcalde, J., Flude, S., Wilkinson, M., Johnson, G., Edlmann, K., Bond, C., Scott, V., Gilfillan, S., Ogaya, X., Haszeldine, R., 2017. Quantifying geological CO2 storage security to

deliver on climate mitigation. Nat. Commun. Curr. Rev. https://doi.org/10.17605/OSF.IO/X59QG

Bachu, S., 2008. CO2 storage in geological media: Role, means, status and barriers to deployment. Prog. Energy Combust. Sci. 34, 254–273. https://doi.org/10.1016/j.pecs.2007.10.001

Bachu, S., Adams, J.J., 2003. Sequestration of CO2 in geological media in response to climate change: Capacity of deep saline aquifers to sequester CO2 in solution. Energy Convers. Manag. 44, 3151–3175. https://doi.org/10.1016/S0196-8904(03)00101-8

Bachu, S., Bennion, B., 2008. Effects of in-situ conditions on relative permeability characteristics of CO2-brine systems. Environ. Geol. 54, 1707–1722. https://doi.org/10.1007/s00254-007-0946-9

Benson, S.M., Cole, D.R., 2008. CO2 sequestration in deep sedimentary formations. Elements 4, 325–331. https://doi.org/10.2113/gselements.4.5.325

Burton, M., Kumar, N., Bryant, S.L., 2008. Time-Dependent Injectivity During CO2 Storage in Aquifers. SPE/DOE Fourteenth Symp. Improv. Oil Recover. Tulsa, Oklahoma, USA 19--23 April 19–23. https://doi.org/10.2118/113937-MS

Chiquet, P., Broseta, D., Thibeau, S., 2007. Wettability alteration of caprock minerals by carbon dioxide. Geofluids 7, 112–122. https://doi.org/10.1111/j.1468-8123.2007.00168.x

Corey, A.T., 1954. The Interrelation Between Gas and Oil Relative Permeabilites, Producers Monthly.

Dávila, G., Cama, J., Luquot, L., Soler, J.M., Ayora, C., 2017. Experimental and modeling study of the interaction between a crushed marl caprock and CO2-rich solutions under different pressure and temperature conditions. Chem. Geol. 448, 26–42. https://doi.org/10.1016/j.chemgeo.2016.10.034

Doughty, C., 2007. Modeling geologic storage of carbon dioxide: Comparison of non-hysteretic and hysteretic characteristic curves. Energy Convers. Manag. 48, 1768–1781. https://doi.org/10.1016/J.ENCONMAN.2007.01.022

Doyen, P.M., 1988. Permeability, conductivity, and pore geometry of sandstone. J. Geophys. Res. 93, 7729–7740. https://doi.org/10.1029/JB093iB07p07729

Dullien, F.A.L., 1992. Porous media : fluid transport and pore structure. Academic Press.

DULLIEN, F.A.L., 1992. Introduction, Porous Media. https://doi.org/10.1016/B978-0-12-223651-8.50006-7

Edlmann, K., Bensabat, J., Niemi, A., Haszeldine, R.S., McDermott, C.I., 2016. Lessons learned from using expert elicitation to identify, assess and rank the potential leakage scenarios at the Heletz pilot CO2 injection site. Int. J. Greenh. Gas Control 49, 473–487. https://doi.org/10.1016/j.ijggc.2016.02.018

Edlmann, K., Edwards, M.A., Qiao, X.J., Haszeldine, R.S., McDermott, C.I., 2015. Appraisal of global CO2 storage opportunities using the geomechanical facies approach. Environ. Earth Sci. 73, 8075–8096. https://doi.org/10.1007/s12665-014-3965-3

Edlmann, K., Haszeldine, S., McDermott, C.I.I., 2013. Experimental investigation into the sealing capability of naturally fractured shale caprocks to supercritical carbon dioxide flow. Environ. Earth Sci. 70, 3393–3409. https://doi.org/10.1007/s12665-013-2407-y

Ennis-King, J., LaForce, T., Paterson, L., Black, J.R., Vu, H.P., Haese, R.R., Serno, S., Gilfillan, S., Johnson, G., Freifeld, B., Singh, R., 2017. Stepping into the Same River Twice: Field Evidence for the Repeatability of a CO2 Injection Test. Energy Procedia 114, 2760–2771. https://doi.org/10.1016/J.EGYPRO.2017.03.1392

Ennis-king, J., Laforce, T., Paterson, L., Dance, T., Jenkins, C., Cinar, Y., 2017. Interpretation of above zone and storage zone pressure responses to carbon dioxide injection in the 2016 CO2CRC field test . Energy Procedia 114, 5671–5679.

https://doi.org/10.1016/j.egypro.2017.03.1706

Eshiet, K., Sheng, Y., 2014. Investigation of geomechanical responses of reservoirs induced by carbon dioxide storage. Environ. Earth Sci. 71, 3999–4020. https://doi.org/10.1007/s12665-013-2784-2

Finsterle, S., 2004. Multiphase Inverse Modeling. Vadose Zo. J. 3, 747. https://doi.org/10.2136/vzj2004.0747

Gamadi, T.D., Sheng, J.J., Soliman, M.Y., Menouar, H., Watson, M.C., Emadibaladehi, H., 2014. An Experimental Study of Cyclic CO2 Injection to Improve Shale Oil Recovery, in: SPE Improved Oil Recovery Symposium. Society of Petroleum Engineers. https://doi.org/10.2118/169142-MS

Garcia, X., Akanji, L.T., Blunt, M.J., Matthai, S.K., Latham, J.P., 2009. Numerical study of the effects of particle shape and polydispersity on permeability. Phys. Rev. E - Stat. Nonlinear, Soft Matter Phys. 80, 1–9. https://doi.org/10.1103/PhysRevE.80.021304

Grigg, R., Svec, R., 2006. CO2 Transport Mechanisms in CO2/Brine Coreflooding. Proc. SPE Annu. Tech. Conf. Exhib. https://doi.org/10.2118/103228-MS

Grigg, R.B., Svec, R.K., 2007. CO2 retention and injectivity changes : laboratory tests. Sixth Annu. Conf. Carbon Capture Sequestration.

Heath, J.E., McKenna, S.A., Dewers, T.A., Roach, J.D., Kobos, P.H., 2014. Multiwell CO2 injectivity: Impact of boundary conditions and brine extraction on geologic CO2 storage efficiency and pressure buildup. Environ. Sci. Technol. 48, 1067–1074. https://doi.org/10.1021/es4017014

Heinemann, N., Stewart, R.J.J., Wilkinson, M., Pickup, G.E.E., Haszeldine, R.S.S., 2016. Hydrodynamics in subsurface CO2 storage: Tilted contacts and increased storage security. Int. J. Greenh. Gas Control 54, 322–329. https://doi.org/10.1016/j.ijggc.2016.10.003

Heinemann, N., Wilkinson, M., Haszeldine, R.S., Fallick, A.E., Pickup, G.E., 2013. CO2 sequestration in a UK North Sea analogue for geological carbon storage. Geology 41, 411–414. https://doi.org/10.1130/G33835.1

Heinemann, N., Wilkinson, M., Pickup, G.E., Haszeldine, R.S., Cutler, N.A., 2012. CO 2 storage in the offshore UK Bunter Sandstone Formation. Int. J. Greenh. Gas Control 6, 210–219. https://doi.org/10.1016/j.ijggc.2011.11.002

Hesse, M.A., Orr, F.M., Tchelepi, H.A., 2009. Gravity currents with residual trapping. Energy Procedia 1, 3275–3281. https://doi.org/10.1016/j.egypro.2009.02.113

Hosa, A., Esential, M., Stewart, J., Haszeldine, S., 2010. Benchmarking worldwide CO2 saline aquifer injections.

Hovorka, S.D., 2013. EOR as Sequestration — Geoscience Perspective.

IEA, 2004. Energy Technology Analysis: Prospects for CO2 Capture and Storage. https://doi.org/10.1016/B978-1-85617-710-8.00010-8

Jerauld, G.R., Salter, S.J., 1990. The Effect of Pore Structure on Hysteresis in Relative Permeability and Capillary Pressure: Pore Level Modeling. Transp. Porous Media 5, 103.

Jikich, S. a., Sams, W.N., Bromhal, G., Pope, G., Gupta, N., Smith, D.H., 2003. Carbon dioxide injectivity in brine reservoirs using horizontal wells. Second Annu. Conf. carbon sequestration, Dev. validating Technol. base to reduce carbon intensity, Alexandria, Virginia 5–8.

Juanes, R., Spiteri, E.J., Orr, F.M., Blunt, M.J., 2006. Impact of relative permeability hysteresis on geological CO2 storage. Water Resour. Res. 42, 1–13. https://doi.org/10.1029/2005WR004806

Kampman, N., Bickle, M., Wigley, M., Dubacq, B., 2014. Fluid flow and CO2-fluid-mineral interactions during CO2-storage in sedimentary basins. Chem. Geol. 369, 22–50.

https://doi.org/10.1016/j.chemgeo.2013.11.012

Koide, H., Tazaki, Y., Noguchi, Y., Nakayama, S., Iijima, M., Ito, K., Shindo, Y., 1992. Subterranean containment and long-term storage of carbon dioxide in unused aquifers and in depleted natural gas reservoirs. Energy Convers. Manag. 33, 619–626. https://doi.org/10.1016/0196-8904(92)90064-4

Larsen A., J.A.. S., 1995. Comparing Hysteresis Models for Relative Permeability in WAG Studies, Sca.

Lewicki, J.L., Birkholzer, J., Tsang, C.F., 2007. Natural and industrial analogues for leakage of CO2 from storage reservoirs: Identification of features, events, and processes and lessons learned. Environ. Geol. 52, 457–467. https://doi.org/10.1007/s00254-006-0479-7

Ma, J., Wang, X., Gao, R., Zeng, F., Huang, C., Tontiwachwuthikul, P., Liang, Z., 2016. Study of cyclic CO2 injection for low-pressure light oil recovery under reservoir conditions. Fuel 174, 296–306. https://doi.org/10.1016/J.FUEL.2016.02.017

McDermott, C.I., Miocic, J.M., Edlmann, K., Gilfillan, S.M.V., 2017. Natural analogue studies, in: Theory and Applications of Transport in Porous Media. https://doi.org/10.1007/978-94-024-0996-3_9

McDermott, C.I.I., Edlmann, K., Haszeldine, R.S.S., 2013. Predicting hydraulic tensile fracture spacing in strata-bound systems. Int. J. Rock Mech. Min. Sci. 63, 39–49. https://doi.org/10.1016/j.ijrmms.2013.06.004

Metz, Davidson, de Coninck, L. and M., 2005. CARBON DIOXIDE CAPTURE AND STORAGE. Cambridge University press, New york.

Meyer, J.P., 2005. Summary of Carbon Dioxide Enhanced Oil Recovery (CO 2 EOR)Injection Well Technology Supporting. Am. Pet. Inst. 63. https://doi.org/http://www.api.org/~/media/Files/EHS/climate-change/Summary-carbon-

dioxide-enhanced-oil-recovery-well-tech.pdf

Morris, J.P., Detwiler, R.L., Friedmann, S.J., Vorobiev, O.Y., Hao, Y., 2011. The large-scale geomechanical and hydrogeological effects of multiple CO2 injection sites on formation stability. Int. J. Greenh. Gas Control 5, 69–74. https://doi.org/10.1016/j.ijggc.2010.07.006

Müller, N., 2011. Supercritical CO2-Brine Relative Permeability Experiments in Reservoir Rocks-Literature Review and Recommendations. Transp. Porous Media 87, 367–383. https://doi.org/10.1007/s11242-010-9689-2

Peng, D.Y., Robinson, D.B., 1976. A New Two-Constant Equation of State. Ind. Eng. Chem. Fundam. 15, 59–64. https://doi.org/10.1021/i160057a011

Pickup, G.E., Mackay, E.J., Heinemann, N., Shariatipour, S.M., 2012. Flow simulation of CO 2 storage in saline aquifers using a black oil simulator. Carbon Manag. Technol. Conf. [CMTC] (Orlando, FL, 2/7-9/2012) Proc. 1, 276–289. https://doi.org/10.7122/151042-MS

Pittman, E.D., 1992. Relationship of porosity and permeability to various parameters derived from mercury injection-capillary pressure curves for sandstone. Am. Assoc. Pet. Geol. Bull. https://doi.org/10.1017/CBO9781107415324.004

Potter, G.F., Hadlow, R.E., Surguchev, L., Research, R., Korbel, R., Haugen, S., Krakstad, O., Patel, P.D., Christman, P.G., Gardner, J.W., 1992. Update of Industry Experience With CO2 Injection. SPE Annu. Tech. Conf. Exhib. 2, 507–513. https://doi.org/10.2118/25075-MS

Rasmusson, K., Rasmusson, M., Tsang, Y., Niemi, A., 2016. A simulation study of the effect of trapping model, geological heterogeneity and injection strategies on CO2 trapping. Int. J. Greenh. Gas Control 52, 52–72. https://doi.org/10.1016/J.IJGGC.2016.06.020

Rutqvist, J., Birkholzer, J.T., Tsang, C.F., 2008. Coupled reservoir-geomechanical analysis

of the potential for tensile and shear failure associated with CO2 injection in multilayered reservoir-caprock systems. Int. J. Rock Mech. Min. Sci. 45, 132–143. https://doi.org/10.1016/j.ijrmms.2007.04.006

Saeedi, A., Rezaee, R., Evans, B., Clennell, B., 2011. Multiphase flow behaviour during CO2 geo-sequestration: Emphasis on the effect of cyclic CO2-brine flooding. J. Pet. Sci. Eng. 79, 65–85. https://doi.org/10.1016/j.petrol.2011.07.007

Saraji, S., Goual, L., Piri, M., Plancher, H., 2013. Wettability of supercritical carbon dioxide/water/quartz systems: Simultaneous measurement of contact angle and interfacial tension at reservoir conditions. Langmuir 29, 6856–6866. https://doi.org/10.1021/la3050863

Schneider, F.N., Owens, W.W., 1976. Relative Permeability Studies of Gas-Water Flow Following Solvent Injection in Carbonate Rocks. Soc. Pet. Eng. J. 16, 23–30. https://doi.org/10.2118/5554-PA

Smart, B.G.D., Somerville, J.M., Edlman, K., Jones, C., 2001. Stress sensitivity of fractured reservoirs. J. Pet. Sci. Eng. 29, 29–37. https://doi.org/10.1016/S0920-4105(00)00088-7

Sohrabi, M., Danesh, A., Tehrani, D., 2005. Oil Recovery by Near-Miscible SWAG Injection. Proc. SPE Eur. Annu. Conf. 24–26. https://doi.org/10.2523/94073-MS

Spiteri, E.J., Juanes, R., 2006. Impact of relative permeability hysteresis on the numerical simulation of WAG injection. J. Pet. Sci. Eng. 50, 115–139. https://doi.org/10.1016/j.petrol.2005.09.004

Suekane, 2008. Geological storage of carbon dioxide by residual gas and solubility trapping. Int. J. Greenh. Gas Control 2, 58–64. https://doi.org/10.1016/S1750-5836(07)00096-5

van Genuchten, M.T., 1980. A Closed-form Equation for Predicting the Hydraulic Conductivity of Unsaturated Soils1. Soil Sci. Soc. Am. J. 44, 892. https://doi.org/10.2136/sssaj1980.03615995004400050002x

Xu, T., Apps, J.A., Pruess, K., 2003. Reactive geochemical transport simulation to study mineral trapping for CO_2 disposal in deep arenaceous formations. J. Geophys. Res. Solid Earth 108, 1–66. https://doi.org/10.1029/2002JB001979

Zhang, Y., Freifeld, B., Finsterle, S., Leahy, M., Ennis-King, J., Paterson, L., Dance, T., 2011. Single-well experimental design for studying residual trapping of supercritical carbon dioxide. Int. J. Greenh. Gas Control. Elsevier Ltd. https://doi.org/10.1016/j.ijggc.2010.06.011

Zoback, M.D., Gorelick, S.M., 2012. Earthquake triggering and large-scale geologic storage of carbon dioxide. Proc. Natl. Acad. Sci. 109, 10164–10168. https://doi.org/10.1073/pnas.1202473109

Supporting information

Number of pages: 10

Number of figures: 5

Number of tables: 3

The supporting information contains further detailed information on:

- Experimental equipment;
- Experimental considerations;
- Experimental processes;
- Sample mineralogy;
- Pore space geometry analysis.
- Experimental relative permeability
- Residual saturation hysteresis model and fitting parameters
- Other field examples

S.1 Experimental Equipment

Figure S.7 presents the rig schematic. The core sample (38mm diameter) is held vertically within a Hassler-type core holder. Fluid entry/exit ports on both the upstream and downstream end platens allow CO_2 and water to be pumped into the bottom of the sample and out of the top. Injection is at the bottom of the sample in order to minimise slug flow, maximise the effects of buoyancy of the CO_2 in relation to any residual brine/water within the sample and minimise the effect of gravity segregation. The core holder is contained within an oven, allowing the temperature of the sample to be controlled and maintained at a constant value. Within the core holder the sample is contained within an elastomer sleeve, and radial pressure is applied to the sample by pressurising confining oil on the outside of the elastomer sleeve using a high pressure hydraulic hand pump. A pair of high pressure syringe pumps at the upstream end of the fluid system control the flow rate of CO_2 through the sample, and a HPLC water pump controls the flow rate of water through the sample. A second pair of high pressure syringe pumps on the downstream end of the fluid system work in constant pressure mode to control the fluid pressure on the downstream end of the core by receiving flow into the syringe pumps (out of the rig) as required in order to maintain a set pressure. The confining pressure is always held at least 5MPa above the fluid pressure to ensure fluid does not bypass the sample along the annulus between the sleeve and sample.

The rig facilitates the measurement and logging of sample and syringe pump temperature; sample confining pressure, fluid pressure both upstream and downstream of the sample along with pressure and flow data from each of the pump controllers (upstream and downstream).

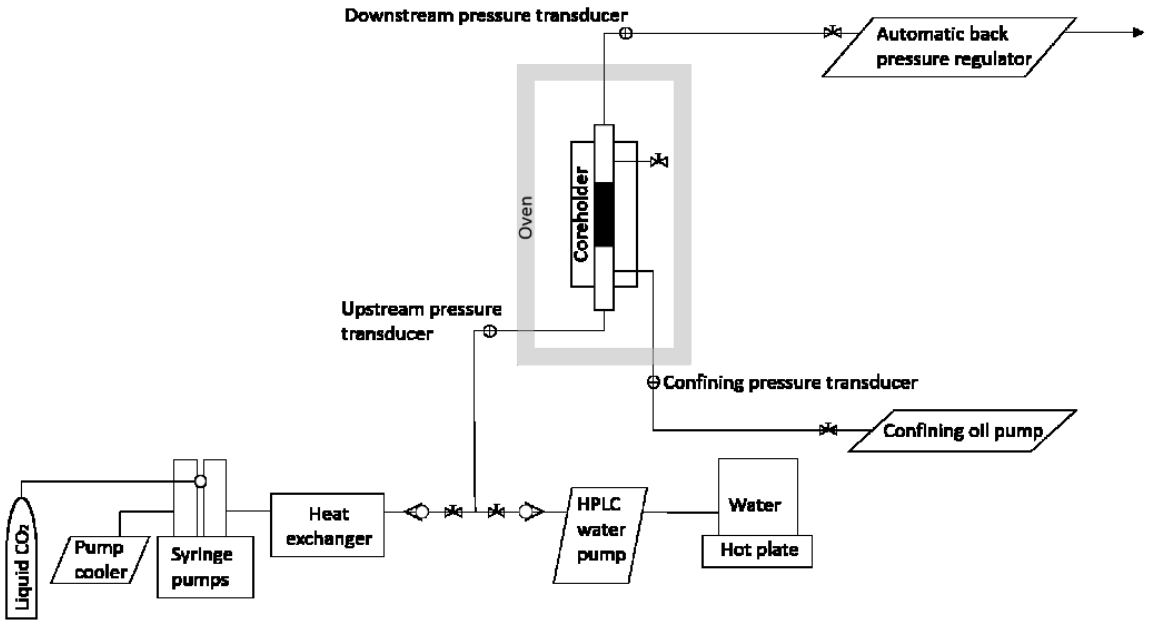

Figure S.7 Rig schematic

S.2 Experimental considerations

The sample and pressure vessel are held within an oven to maintain a constant temperature and the injection fluids pass through a heat exchanger and heated pipework to ensure the water and scCO_2 are delivered to the sample at 40^{o}C, to minimise any potential for thermal shock

The fluid pumps (both water and CO_2) are designed for high temperature, pressure and supercritical CO_2 conditions and all wetting parts within the system are in 316 stainless steel or PEEK to limit corrosion on exposure to brine and supercritical CO_2.

The water is deionised and unsaturated with respect to CO_2

The sandstone sample was vacuum saturated in deionised water for 4 weeks and weighed to ensure the maximum saturation possible was reached and placed into the experimental apparatus. When the samples were removed from vacuum saturation in water and loaded into the test cell they were exposed to the atmosphere and it is possible that suction and imbibition forces enabled air to enter into sandstone. Quick sample transfer and an initial cycle of water injection to steady state equilibrium will ensure any air within the sample is

minimised. Careful preparation, control and monitoring of the sample, equipment and experimental procedure was undertaken to minimise the risk of experimental errors.

S.3 Experimental process

Table S.1 presents the detailed experimental process cycle for the flow experiments and Table S.2 presents the exact timings of the flow cycles.

Table S.1 Methodology and flow process cycle for the flow experiments

Step 1	**Sample loading**: The saturated sample was placed into the flow cell and the confining pressure raised to 2900psi (20MPa), the fluid flow heat exchanger was set to 40^{o}C and the heating tapes turned on and the temperature was monitored inside and outside the flow cell with an LCD temperature logger until the temperature was held constant at 40^{o}C.
Step 2	**Equipment setup**: The flow rates for both water and CO_2 pumps were set to 1ml/min and the fluid pressure was set to 1450psi (10MPa), controlled throughout the experiment by the downstream ISCO syringe pump under pressure control.
Step 3	**Cycle 1: Initial flow setup / 1st water flow**: The water pump was set to flow at 1ml/min and the water flow was left to reach steady state, which took approximately 20 minutes until the differential pressure of the flow through the sample had stabilised. The first water flow section of cycle 1 then began and was run for 15 minutes, maintaining the steady state of flow equilibrium. As the sample is water wet this cycle can be considered the **primary imbibition phase**.
Step 4	**Cycle 1: CO_2 flow**: Simultaneously the CO_2 pump was switched on and the CO_2 needle valve was opened at the same time as the water needle valve was closed and the water pump was switched off as quickly as possible, aiming to minimise pressure losses during the changeover. CO_2 flow rate from the pump proceeded at 1ml/min and ran until a steady state of flow equilibrium was reached and maintained for at least 15 minutes. This is the **primary drainage phase** where the non-wetting fluid displaces the wetting fluid, decreasing the wetting phase saturation.
Step 5	**Cycle 2: Water flow**: After the 1st CO_2 flow cycle was complete, simultaneously the water pump was switched on and the water needle valve was opened at the same time as the CO_2 needle valve was closed and the CO_2 pump stopped to start the 2nd water cycle which ran until a steady state of flow equilibrium was reached and maintained for at least 15 minutes. This is the **imbibition (secondary) phase** when the wetting fluid is added, increasing the wetting phase saturation.
Step 6	**Cycle 2: CO_2 flow**: After the 2nd water cycle was complete, simultaneously the CO_2 pump was switched on and the CO_2 needle valve was opened at the same time as the water needle valve was closed and the water pump was switched off to start the 2nd CO_2 cycle which ran until a steady state of flow equilibrium was reached and maintained for at least 15 minutes. This is the **secondary drainage phase** when the non-wetting fluid again displaces the wetting fluid.
Step 7	**Subsequent cycles**: This sequence was repeated for six cycles of alternating CO_2 and water injections. The flow experiments ran for approximately five hours.

Table S.2 Time increments of the flow cycles

Cycle	Flow	Timing of cycle (minutes)	Duration of cycle (minutes)	Median time (minutes)
1	Water	0-17	17	8.5
1	CO_2	17-33	16	25
2	Water	33-49	16	41
2	CO_2	49-72	23	60.5
3	Water	72-94	22	83
3	CO_2	94-115	21	104.5
4	Water	115-135	20	125
4	CO_2	135-162	27	148.5
5	water	162-184	22	173
5	CO_2	184-209	25	196.5
6	Water	209-236	27	222.5
6	CO_2	236-262	26	249

S.4 Fell sandstone mineralogy

Table S.3 presents the mineral abundances in the Fell sandstone before and after the cyclic flow experiment as determined by XRD, Figure S.8 presents representative SEM images and Figure S.9 presents the XRD and optical microscopy results for the Fell sandstone for both the pre and post flow.

Table S.3 % mineral abundances in the Fell sandstone before and after the cyclic flow experiment

Mineral	Mineral wt% before cyclic flow	Mineral wt% after cyclic flow
Quartz (SiO2)	92.9	94.0
Calcite (CaCo3)	0.1	0.1
Albite	0.6	0.7
Anorthite	0.6	0.4
Illite $(K,H_3O)(Al,Mg,Fe)_2(Si,Al)_4O_{10}[(OH)_2,(H_2O)]$	1.3	1.0
Kaolinite $Al_2Si_2O_5(OH)_4$	1.0	0.8
Chlorite $(Mg,Fe)_3(Si,Al)_4O_{10}$	0.4	0.3
Microcline $KAlSi_3O_8$	2.1	2.1
Orthoclase	0.4	0.2
Muscovite $KAl_2(AlSi_3O_{10})(F,OH)_2$ or $(KF)_2(Al_2O_3)_3(SiO_2)_6(H_2O)$	0.4	0.3

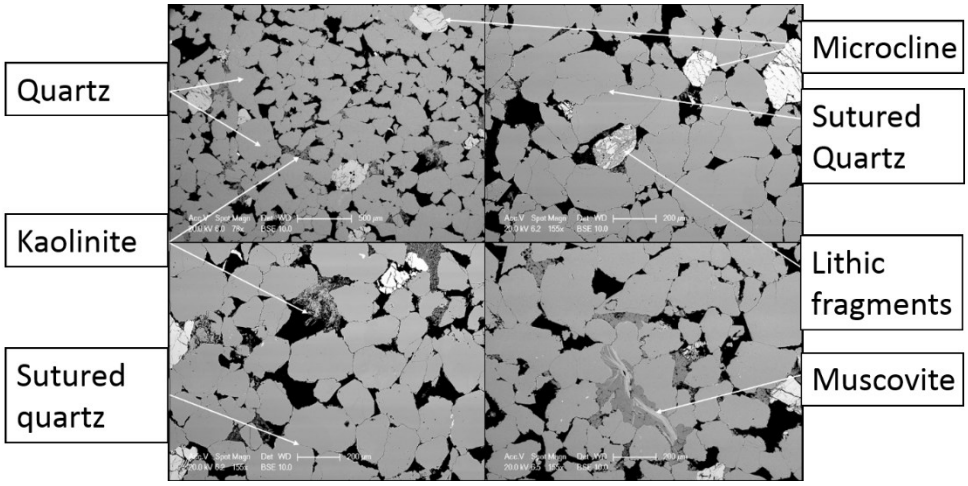

Figure S.8 Representative Scanning Electron Microscope images of the Fell Sandstone showing a predominantly quartz-rich sandstone with some alteration of microcline to kaolinite. The individual quartz grains are closely packed and with some interlocking (suture) textures observed.

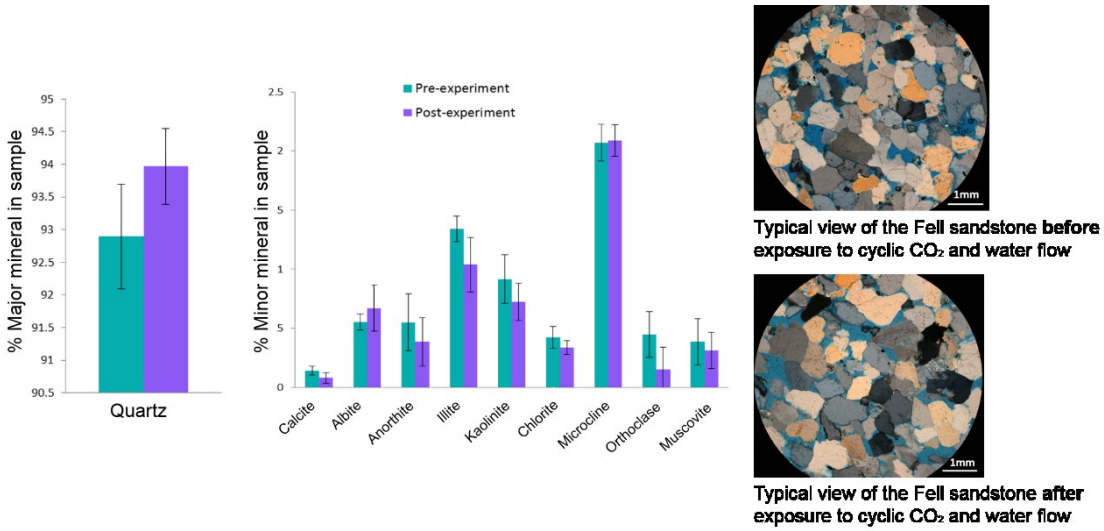

Figure S.9 Pre and post cyclic flow thin sections and X-Ray diffraction results for the Fell Sandstone. Error bars are calculated from the standard deviation of the five repeat measurements for each sample.

S.5 Fell sandstone pore space geometry analysis

The typical pore network of the fell sandstone as seen in optical microscope images, Figure S.10A is shown to have a mixture of irregular pore sizes ranging in size from 100μm to 400μm, that are generally interconnected. Image J was used to calculate the pore size distribution from the optical microscope images and the results, Figure S.10B, confirm the pore size range from 100μm to 400μm.

Pore shape analysis was calculated on four images over three magnifications obtained from the optical microscope (OM) and backscattered SEM (BS) images, using:

$$\gamma = P/(2\sqrt{\pi A})$$

Where P is the pore perimeter (μm), A is the pore area (μm^2) and γ is a dimensional value that represents the pore geometry. A spherical pore is seen as a circle in a 2D image and would have a γ value equal to one. Pore spaces will become more complex and diverging as the γ value increases. Figure S.10C shows the calculated pore size diameter measured against γ. The dotted line represents the median value taken for each pore space range and shows that the smaller pores have lower γ values, suggesting that the smaller pores are simple and well rounded; and become more complex with an increase in size. This figure shows that the majority of the pores are between 100μm and 400μm, with a γ value of 4 and below indicating the pore space is relatively simple and well rounded.

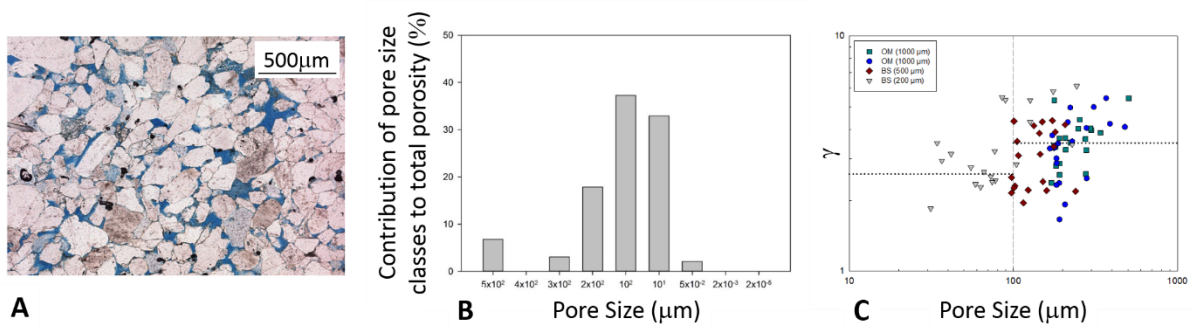

Figure S.10 Optical microscope photograph of the Fell sandstone (pore space is shown in blue); B. boxplot of the pore size distribution calculated using ImageJ and C. plot of pore shape parameter (γ) with the macro pore space (>10 µm) for individual pores of the Fell sandstone.

S.6 Experimental relative permeability

The effective permeability (k) of each fluid phase was then calculated for each cycle using:

Darcy's equation:

$$k = QmL / DPA$$

Where Q is the volumetric flow rate in m^3s^{-1} ($1.666667x10^{-8}$ m^3s^{-1} for water and $2.656x10^{-8}$ m^3s^{-1} for CO_2), μ is dynamic viscosity in Pa.s (6.53x10-4 Pa.s for water and 4.82x10-5 Pa.s for CO_2), L is sample length in m (0.08m), A is the cross sectional area of the sample in m (0.00113m) and ΔP is the measured pressure difference across the sample in Pa

The relative permeability could then be calculated using the following equation:

Relative permeability = Effective permeability / intrinsic permeability

Figure S.11 presents the results of the relative permeability calculations for each fluid for ach cycle.

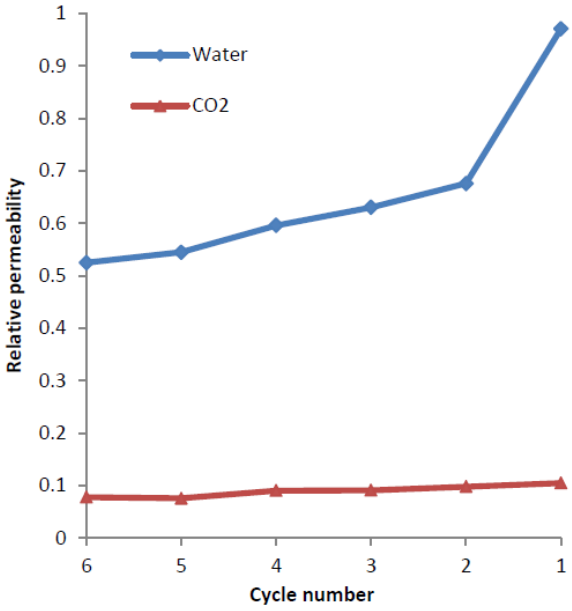

Figure S.11 The relative permeability for the water and scCO₂ phases for the Fell Sandstone. The cycle number is used as a proxy for the water saturation of the sample with cycle 1 having 100% saturation.

S.7 Residual saturation hysteresis model and fitting parameters

The hysteresis model for relative permeability and capillary pressure referenced in the first part of the numerical modelling is described by Doughty (reference [40] in main manuscript). The model defines four branches of the capillary pressure curve: primary drainage and primary wetting curves, a first order scanning wetting curve, a second order scanning drainage curve, and a third order scanning wetting curve. The lack of further branches may relate to the observed limits of the model in reproducing the effect of six cycles of alternating CO_2 and water injection.

The capillary pressure P_c has the form

$$P_c = -P_0^i \left[\left(\frac{S_l - S_{lmin}}{1 - S_{gr}^{\Delta} - S_{lmin}} \right)^{-\left(\frac{1}{m^i}\right)} - 1 \right]^{1-m^i}$$

Where i is the index for the branch of the capillary pressure curve (w for wetting and d for drainage), S_l is the liquid saturation and $P_0^i, m^i$and S_{lmin} are parameters. During drainage, $S_{gr}^{\Delta} = 0$, while during wetting

$$S_{gr}^{\Delta} = \frac{1 - S_l^{\Delta}}{1 + \left(\frac{1}{S_{grmax}} - \frac{1}{1 - S_{lr}}\right)\left(1 - S_l^{\Delta}\right)}$$

where S_{grmax} is a material parameter. The turning point saturation S_l^{Δ} (the liquid saturation at the transition from primary drainage to imbibition) and the residual gas saturation S_{gr}^{Δ} depend on the saturation history in that location. The relative permeability to liquid, k_{rl} is given by

$$k_{rl} = \sqrt{\overline{S_l}} \left[1 - \left(1 - \frac{\overline{S_{gt}}}{1 - \overline{S_l^{\Delta}}} \right) \left(1 - \left(\overline{S_l} + \overline{S_{gt}} \right)^{\frac{1}{m_l}} \right)^{m_l} - \left(\frac{\overline{S_{gt}}}{1 - \overline{S_l^{\Delta}}} \right) \left(1 - \left(\overline{S_l^{\Delta}} \right)^{1/m_l} \right)^{m_l} \right]^2$$

And the relative permeability to gas, k_{rg} is given by

$$k_{rg} = k_{rgmax} \left(1 - \left(\overline{S_l} + \overline{S_{gt}} \right) \right)^{\gamma} \left(1 - \left(\overline{S_l} + \overline{S_{gt}} \right)^{\frac{1}{m_g}} \right)^{2m_g}$$

Where

$$\overline{S_l} = \frac{S_l - S_{lr}}{1 - S_{lr}}$$

$$\overline{S_l^{\Delta}} = \frac{S_l^{\Delta} - S_{lr}}{1 - S_{lr}}$$

$$\overline{S_{gt}} = \frac{S_{gr}^{\Delta}\left(S_l - S_l^{\Delta}\right)}{\left(1 - S_{lr}\right)\left(1 - S_l^{\Delta} - S_{gr}^{\Delta}\right)}$$

Details of implementation, and interpolation in the regions beyond the end-points are discussed in Doughty (reference [40] in main manuscript).

The fitted values of the parameters from iTOUGH2 presented in Figure 4 of the main manuscript are as follows:

Table S.4: Parameters for hysteretic relative permeability and capillary pressure functions fitted to experimental data

Parameter	Fit to 4 cycles	Fit to 6 cycles	Fit to 6 cycles with 50% solubility
m_l	0.859	0.677	0.849
S_{lr}	0.0496	0.0474	0.0543
S_{grmax}	0.533	0.365	0.532
γ	0.287	0395	0.201
m_g	0.631	0.549	0.739
m^d	0.485	0.323	0.333
P_0^d (kPa)	22.8	35.1	26.4

These parameters were selected for adjustment because they had the greatest impact on the fit. The other necessary parameters were fixed at the following values: $k_{rgmax} = 0.95$, $S_{lmin} = 0.01$, $m^w = 0.412$, $P_0^w = 14.3$ kPa.

S.8 Other field examples

The second field example is the Heletz CO_2 injection project in Israel. They are planning to conduct experiments on residual trapping and how to enhance trapping by different modes of injection including cyclic CO_2-water injection, this project has not yet performed the field experiments. However, simulations of enhanced trapping injection strategies and their impacts on pressure in the reservoir have been conducted and can be found in reference [64]

in main manuscript. Relative to the conventional injection, all scenarios enhanced the trapping (primarily due to increased residual trapping) in the short term (4 day). Hence the pressure responses above the conventional injection strategy are observed to be due to the relative amount of increased residual trapping observed in each scenario.